Plasma Channels and Laser Pulse Tailoring for GeV Laser-Plasma Accelerators

M. C. Downer, C. Chiu, M. Fomyts'kyi, E. W. Gaul, F. Grigsby, N. H. Matlis, B. Shim, P. J. Smith, and R. Zgadzaj

Citation: AIP Conference Proceedings **647**, 654 (2002); doi: 10.1063/1.1524920
View online: http://dx.doi.org/10.1063/1.1524920
View Table of Contents: http://scitation.aip.org/content/aip/proceeding/aipcp/647?ver=pdfcov
Published by the AIP Publishing

Plasma Channels and Laser Pulse Tailoring for GeV Laser-Plasma Accelerators

M. C. Downer, C. Chiu, M. Fomyts'kyi, E. W. Gaul, F. Grigsby, N. H. Matlis, B. Shim, P. J. Smith and R. Zgadzaj

University of Texas at Austin, Department of Physics, Austin, TX 78712

Abstract. We have demonstrated distortion-free guiding of 1 TW pulses at near relativistic intensity (0.2 x 10^{18} W/cm^2) over 60 Rayleigh lengths at 20 Hz repetition rate in a preformed helium plasma channel. As steps toward efficient channeled Laser Wakefield Acceleration up to the dephasing limit, we have upgraded our laser system from 1 to 4 TW, adapted femtosecond interferometric diagnostics to probe plasma density fluctuations inside the channel, and developed detailed strategies for managing ionization distortions at the channel entrance and exit at the upgraded intensity. We also report simulations, and preliminary experiments, that explore a strategy for Raman-seeding laser pulses to coherently control both unchanneled and channeled LWFA in order to lower the laser energy threshold and increase the repetition rate of electron pickup and acceleration.

PLASMA CHANNELS FOR TERAWATT LASER PULSES

Plasma waveguides capable of guiding relativistically intense fs laser pulses *without optical distortion* are essential to developing GeV-scale Laser Wakefield (LWF) Accelerators [1]. Several groups have demonstrated guiding of pulses at intensities ~ 10^{17} *W/cm*^{2} in hollow [2] or gas-filled [3] solid capillaries by various methods, as summarized in the plenary talk by A. Zigler. Recent work at Texas, on the other hand, has adopted a channel generation method pioneered by Milchberg and co-workers [4], in which the waveguide forms from the expanding cylindrical shock wave around a plasma filament heated by a powerful line-focused laser pulse. Although this approach requires an additional dedicated laser for channel generation, it has two advantages over capillary-based methods. First, the channels can be replenished indefinitely, since there are no solid boundaries that are subject to damage. Secondly, these channels routinely support stably-propagating modes as small as $w_0 \sim 8\ \mu m$, thus enabling fully relativistic guided intensity (10^{18} *W/cm*^{2}) to be achieved at pulse energies (*0.02 – 0.2 J*) that can be produced by high repetition rate ($\geq$ *10 Hz*), table-top *10-100 fs* laser systems. Capillary-based channels, on the other hand, to date have guided larger modes ($20 < w_0 < 30\ \mu m$), for which national-laboratory-scale, multi-joule laser systems will be required to reach the same intensity. This will limit performance to low repetition rates, although flatter acceleration fronts will be possible.

Distortion-Free Guiding of 1 TW pulses over 60 Rayleigh Lengths

We first summarize recently reported results [5] which achieved an intensity-length product of 0.2×10^{18} *W/cm*^{2} $\times$ *1.5 cm* for distortion-free guiding. We generated our channels in a

CP647, *Advanced Accelerator Concepts: Tenth Workshop*, edited by C. E. Clayton and P. Muggli

backfill of He gas (*300-700 Torr*) using a modification of the method of Milchberg *et al.* [4], who line-focused *~100 ps, ~0.3 J Nd:YAG* laser pulses to intensities of $\sim 10^{13}$ *W/cm*^{2} into a gas using an axicon (see Fig. 1a). This intensity readily field-ionizes high-*Z* gases (e.g. Ar, N_2), thus initiating the channel-forming process, but forms an *incompletely-ionized* channel, in which relativistically intense pulses suffer ionization-induced phase distortion (during guiding) and defocusing (when entering the channel). Indeed we observe distorted exit mode and spectrum (see Fig. 1c) and < *5%* throughput when we attempt to guide a pulse at $\geq 10^{17}$ *W/cm*^{2} through a N_2 channel.

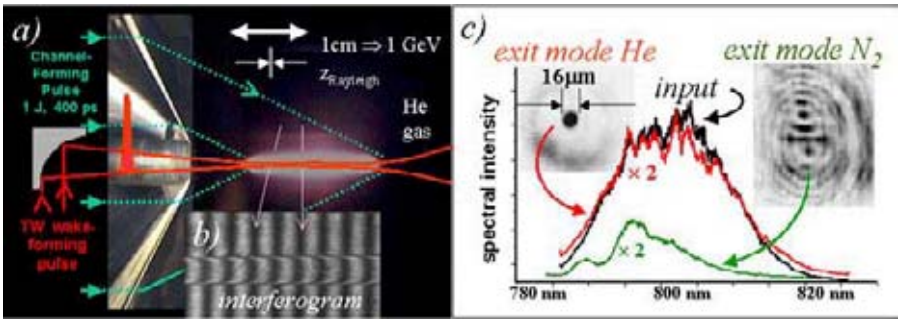

FIGURE 1. Demonstration of distortion-free guiding of 0.2×10^{18} *W/cm*^{2} through a fully-ionized He plasma channel. **(a)** photo of conical axicon and fluorescencing filament from plasma heated by line-focused *1 J, 400 ps* Nd:YAG channel-forming pulse. The TW Ti:Sapphire pulse is coupled into the channel through the hole in the center of the axicon. **(b)** transverse interferogram of plasma channel *3 ns* after line focus. Abel inversion of this interferogram reveals a density depression on axis which guides the Ti:sapphire pulse over *1.5 cm* . **(c)** mode and spectra of intense Ti:S pulse exiting channel. Mode exiting He channel is cylindrically symmetric (upper left) and spectrally indistinguishable from input (upper two spectra); mode exiting N_2 channel is spatially disorted (upper right), spectrally blue-shifted and severely attenuated (*~0.05*) by poor coupling (bottom spectrum).

To overcome these problems, we formed channels in a He backfill. A backfill provides more *uniform* gas density than a jet, essential for obtaining uniform or controllably tapered channel diameter. Use of He gas minimizes ionization-induced distortions *inside* the channel, where (like H_2) it can be fully–ionized, *and* in the entrance/exit regions, where (unlike H_2) its high ionization threshold ($\sim 10^{15}$ *W/cm*^{2}) suppresses ionization until the focusing *fs* pulse is nearly inside the channel. Unfortunately, this high threshold also prevents the channel-forming YAG pulse from field ionizing neutral He. However, we succeeded in forming excellent He channels with 3 modifications of the procedure of Ref. [4]: (i) pre-ionizing He with a discharge to provide seed electrons; (ii) lengthening the channel-forming pulse to 400 ps to increase inverse Bremsstrahlung heating; (iii) amplifying the channel-forming pulse to *1 J* to maintain line-focused intensity $\sim 10^{13}$ *W/cm*^{2} [3]. Transverse interferometry (Fig. 1b) confirms that the resulting channels are fully ionized. Most importantly, *800nm, 80 fs, 50 mJ* pulses focused to beam diameter *16 μm* at the channel entrance by an *f/8* off-axis parabolic mirror, exit the channel with ~ *50%* of their incident energy, undistorted transverse mode and undistorted spectrum (Fig. 1c). Best results are obtained by coupling *~3 ns* after the Nd:YAG line-focus, to enable formation of a channel of axial density $n_e(r=0) = 4 \times 10^{18}$ *cm*$^{-3}$, radius *40 μm*.

Time-resolved frequency-domain interferometry in a plasma channel

An essential step in the development of channeled LWFA will be accurate characterization of the plasma wave structure using time-delayed probe pulses that co-propagate with the plasma

wave and its driver pulse. Past work by our group and others has used double-probe frequency domain interferometry (FDI) for sensitive measurement of longitudinal and radial profiles of wakefields [6]. To implement FDI in a channel of length $L \geq 1$ *cm*, three new features come into play. First, since group velocity walk-off of pump and probe pulses must be $\leq \lambda_p/4$ to avoid washing out the wave structure, $\lambda_{probe} - \lambda_{pump} \leq \lambda_p^3/4\pi L\lambda_{pump}$ is required. As an example, for $\lambda_{pump} = 0.80\ \mu m$ in a channel with axial density $n_e(r=0) = 3 \times 10^{18}\ cm^{-3}$, we need $0.78 \leq \lambda_{probe} \leq 0.82\ \mu m$. Second harmonic or continuum probes will therefore be of little use; for practical purposes $\lambda_{probe} \approx \lambda_{pump}$ is required. Polarization is therefore the only means for discriminating transmitted probe(s) from pump pulses. Second, coupling one pulse efficiently into a small channel entrance is already difficult; coupling 2 or more probes multiplies the difficulty. Third, photon acceleration [7] of the trailing probe by the LWF will become significant, thus reducing fringe contrast [8].

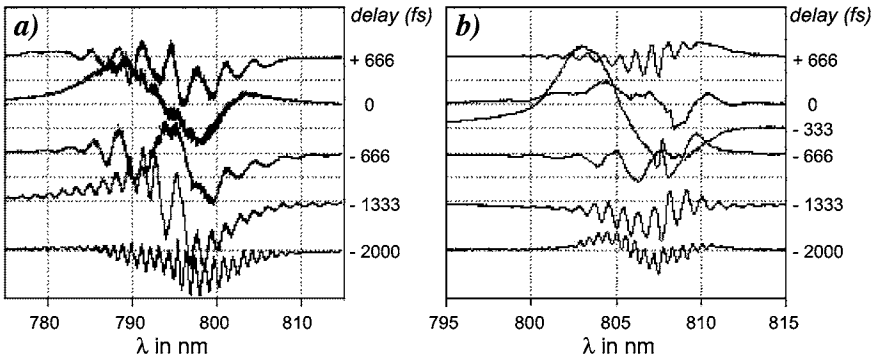

FIGURE 2. Spectra of probe pulses after propagation through 1.5 cm plasma channels formed in (a) *700 Torr* He or (b) *100 Torr* N_2, at time delays $-2000 < \Delta t < +666$ *fs* from peak of intense, orthogonally-polarized guided pulse, normalized to undistorted pulse spectrum. Oscillations with period $\omega\Delta t$ are produced by frequency domain interference between probe pulse and depolarized scattered pump light.

In order to test these issues, we performed pump-probe experiments in a fully-ionized channel formed in *700 Torr* He with $I_{pump} \approx 10^{17}\ W/cm^2$, and in partially-ionized channels formed in *100 Torr* N_2 with $I_{pump} \approx 10^{16}\ W/cm^2$. We used $\lambda_{probe} = \lambda_{pump} = 800\ nm$ to avoid group-velocity walk-off and $\boldsymbol{E}_{probe} \perp \boldsymbol{E}_{pump}$ to discriminate transmitted probe from pump spectra. Even though only a single probe pulse was intentionally injected, a second reference pulse was provided "for free" by *~0.1%* depolarization of the pump pulse. This greatly alleviates the difficulty of injecting multiple probes. Because of full channel ionization, the latter pulse coincided temporally and spectrally with the parent pump pulse. Frequency-domain interference between this pulse and the probe of comparable intensity at time delay Δt produced fringes $E_{probe}E_{depol.\text{-}pump}\cos\omega\Delta t$ that are clearly visible in Fig. 2. The variable fringe period $(\Delta t)^{-1}$ agreed with an independently calibrated Δt, and thus will provide convenient *in-situ* calibration of Δt in future experiments. Fringe contrast was stable and reproducible from shot-to-shot. For the data in Fig. 2, the probe was adjusted to *~3×* the energy of the depolarized pump reference pulse. The undistorted reference spectrum was then subtracted to produce the differential FDI spectra shown for several representative time delays in the interval $-2000\ fs < \Delta t < 666\ fs$.

A small blue shift of the trailing probe is evident at $\Delta t \leq 0$ in the He channel (Fig. 2a), and at $\Delta t = -333\ fs$ in the N_2 channel (Fig. 2b), even though no shift was observed in the transmitted pump (see Fig. 1c for He channel; for the N_2 channel I_{pump} is *~10×* lower than for data in Fig.

1c). At these guided intensities, ionization fronts occur well in the leading edge of the guided pulse, and thus blue-shift only a small fraction of its energy, even if present. On the other hand, because pump and probe group velocities are identical, the time-advanced ($\Delta t < 0$) probe "rode" the pump ionization front, and characterized it more sensitively through its cumulative blue-shift $\Delta\omega \sim \int^L (dn_e/dt)dz$. The shift did not vary with channel length, proving that it originated primarily from residual ionization in the entrance/exit regions. For the He channel, the probe shift became undetectable for channels generated in $p < 500$ *Torr* He gas. While this small residual ionization did not noticeably affect pump propagation, its detection demonstrates the sensitivity of a properly timed, group-velocity-matched probe. The results also show that a blueshift (*i.e.* photon acceleration) less than the probe pulse bandwidth does not significantly reduce FDI fringe contrast. Thus FDI remains a viable technique for probing low amplitude channeled LWFA.

The depolarized light responsible for the reference pulse scaled linearly with pump intensity, suggesting that it results from linear laser-plasma interaction. However, linear Thomson scatter cannot produce an orthogonal field component in the forward direction. Most likely, it develops as coupled light evolves to a confined eigen-mode of a cylindrical waveguide, which typically contain substantial orthogonal polarization components in order to satisfy cylindrical boundary conditions [9]. Imperfections in the waveguide may also contribute to depolarization. Small intentional misalignment of the analyzer can transmit additional pump light, although higher probe intensity is then needed to maintain good fringe contrast. The above results were obtained with the polarization analyzer adjusted for minimum pump transmission, which enables the lowest probe intensity to be used.

Efficient Coupling of Multi-Terawatt Laser Pulses into a Plasma Channel

In order to generate high amplitude wakefields inside the channel, guided intensity $I_{guided} = \eta P/\pi w_0^2 \geq 0.8 \times 10^{18}$ *W/cm*^{2} will be required. For guided mode area $\pi w_0^2 = 2 \times 10^{-6}$ *cm*^{2} (as shown in Fig. 1c) and coupling efficiency $\eta \approx 0.5$ (as observed in [5]), incident peak power $P =$ *4 TW* will be required. We have therefore recently upgraded our Ti:S laser system from *1* to *4 TW* by adding a new amplification stage to produce *0.2 J, 50 fs* pulses at *800 nm*.

However, upgrading the laser is only half the battle of achieving $I_{guided} \geq 0.8 \times 10^{18}$ *W/cm*^{2}. In addition, the channel entrance must be re-designed to maintain high η. For a channel formed in a He backfill [5], the *4 TW* pulse will begin ionizing neutral He gas, and thus defocusing, *5 mm* or more from the ionized channel entrance, similar to the situation for a *1 TW* pulse approaching a N_2 channel. We have already observed that coupling efficiency is severely degraded in the latter case (Fig. 1c). Generating channels in a gas jet alleviates this problem [10], at the cost of uncontrolled density non-uniformity across the jet. We will therefore generate plasma channels in a differentially-pumped cell to maintain uniform, controlled density within the cell. Propagation calculations [11] show that the gas density must drop abruptly from its plateau value ($n_{max} \sim 10^{19}$ *atoms/cm*^{3}) to $\sim .01 n_{max}$ within *1-3 mm* (depending on gas species) of the entrance aperture in order for a *4 TW* pulse to focus to $\sim 10^{18}$ *W/cm*^{2}. Accurate characterization and control of the gas profile near the entrance aperture are therefore critical to successful guiding at relativistic intensity.

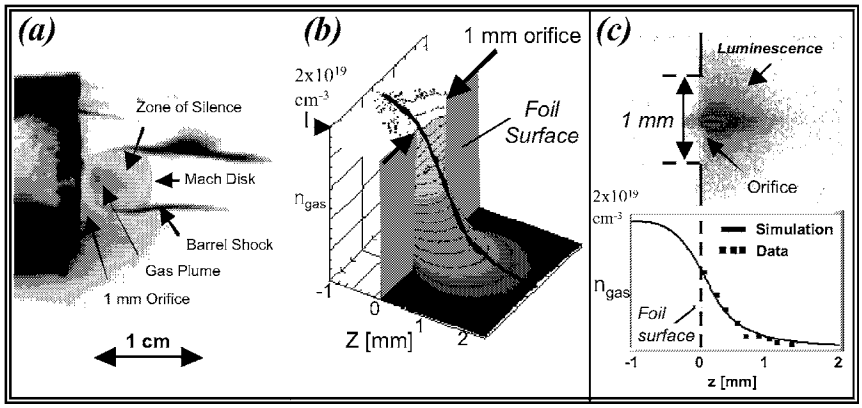

FIGURE 3. **(a)** Mie scatter image of the structure of the gas plume within *1 cm* of the *1 mm* diameter orifice of a cell containing *310 Torr* He. Supersonically flowing zone of silence is bounded by Mach disk and barrel shock. **(b)** Direct Monte Carlo (DMC) simulation of gas profile within *1 mm* of the orifice of the same cell. **(c)** Measurement of gas density within *1-2 mm* of the orifice. Picture at top shows single-shot transverse image of luminescence in gas plume excited by laser focused into orifice. Bottom graph plots luminescence intensity along symmetry axis of hole, normalized to constant laser intensity (data points), compared to lineout of DMC simulation results (curve).

Fig. 3a shows the overall structure of the gas plume within ~ *1 cm* of the orifice (diameter $d = 1$ *mm*) of our differentially-pumped cell pressurized to *310 Torr* helium. This image was recorded by transversely imaging Mie scattering of a helium-neon laser. Scattering was enhanced by leaking into the flow a trace of acetone, which clustered upon cooling in the expanding plume. A supersonically flowing "zone of silence" bounded by "barrel" and "Mach disk" shocks is clearly visible. Indeed, supersonic flow is expected whenever the ratio P_0/P_B of cell to background pressure exceeds the critical value $(P_0/P_B)_{crit} = ((\gamma+1)/2)^{\gamma/(\gamma-1)}$, which is less than 2.1 for all gases [12]. The Mach disk occurs at distance $x_M = 0.67\ d\ (P_0/P_B)$ from the orifice, and provides a sensitive diagnostic of P_0/P_B. As long as P_B is less than a few Torr (exact value depends on gas species) an intense pulse propagates through the zone of silence and Mach disk with negligible distortion. However, within *1-2 mm* of the orifice, gas pressure climbs abruptly to P_0, as shown by the direct Monte Carlo simulation [13] in Fig. 3b. This simulation confirms excellent density uniformity inside the aperture, and an abrupt step in density with scale length ~d outside. The density profile immediately outside the aperture was measured by transversely imaging luminescence induced by a tightly focused laser, as shown in Fig. 3c. The top figure shows a single-shot luminescence image. The laser focus was then translated along the axis in *~0.1 mm* increments to record the data points shown in the bottom graph. These data points agree very well with an axial lineout (solid curve) of the Monte Carlo simulation, confirming that the density drops abruptly within *~1 mm* of the aperture.

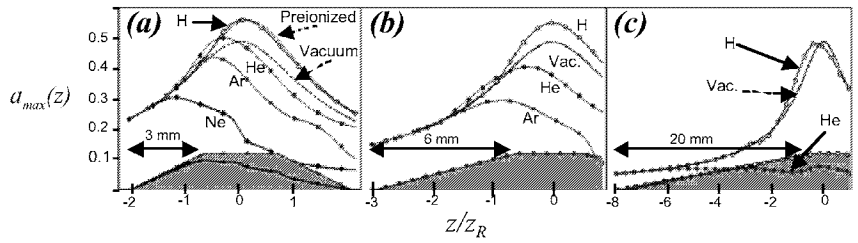

FIGURE 4. Calculated axial normalized vector potential $a(r=0,z)$ at the peak of a *30 fs, 5 TW, 0.8 μm* laser pulse focused at *f/30* into the trapezoidal profile of neutral H, He or Ar gas shown at bottom (gray), with entrance/exit ramps of length **a)** *3 mm*, **b)** *6 mm* or **c)** *20 mm* and plateau density 2×10^{18} cm^{-3}.

Figure 4 shows the results of several simulations [11] of the propagation of intense, ultrashort laser pulses through ionizing gas profiles similar in scale length to those measured above. The code simultaneously and self-consistently solves Maxwell's equations, the Ammosov-Delone-Krainov (ADK) field ionization equations [14], and the relativistic cold plasma equations. The axial normalized vector potential $a(r=0,z)$ for a *5 TW, 30 fs, 0.8 μm* laser pulse focused at *f/30* into a trapezoidal profile of neutral H, He, Ne or Ar gas (shaded region at bottom) with plateau density 2×10^{18} cm^{-3} is plotted in comparison to the vacuum focus (dashed curves). At this relatively low density, entrance and exit ramps *3 mm* long enable the full vacuum focused intensity to be reached in H, He and Ar (panel (*a*)). When entrance/exit ramps lengthen to *20 mm*, however, vacuum intensity is reached only in H (panel (*c*)). For higher plateau density, tighter focus and/or shorter ramps are required. Ionization of the plateau region (as would occur when a channel forms there) and/or partial pre-ionization of the ramps relax the requirements on the ramp lengths considerably. A number of such examples are presented in [11]. These simulations, together with the gas profile measurements above, suggest that it should be possible to couple a *4 TW* pulse efficiently into a properly designed differentially-pumped H or He channel cell.

RAMAN-SEEDING: TOWARD KHZ LWFA

In addition to channeled LWFA, our group is investigating schemes for tailoring the driving pulse to achieve more efficient, higher repetition rate LWFA than is currently possible. The advent of kHz repetition rate terawatt lasers [15] has opened the possibility of generating high average current MeV-electron beams by self-modulated (SM) LWFA, for potential applications in radiation oncology [16], nuclear activation of rare isotopes [17] and beam injection into conventional accelerators [18]. Currently, however, such lasers can be focused only to mildly relativistic ($a_0 = eE_0/(m\omega c) < 0.5$) intensities, and thus cannot efficiently drive the forward Raman instability responsible for low-emittance, nano-Coulomb bunches that have been generated with $\leq$ *10 Hz* repetition rate lasers. Here we describe PIC simulations and experimental plans to explore a Raman-seeding mechanism, originally proposed by Fisher and Tajima [19], in which a main pulse $E_y(\omega)$ is "seeded" by a weak co-propagating, superposed pulse $E_y'(\omega_{seed})$ of frequency $\omega_{seed} = \omega - \omega_p$. A seed as small as $0.01\ |E_y(\omega)|$ greatly enhances the trailing wakefield generated in a plasma of density ω_p compared to the unseeded case [19]. In this work, we additionally simulate the intensity- and frequency-dependence of wakefield enhancement, and the yield and spectrum of accelerated electrons.

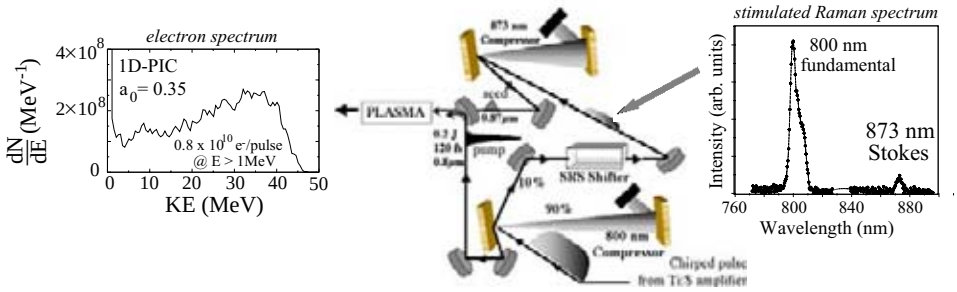

FIGURE 5. Center: experimental setup for Raman-seeded SM-LWFA as described in text. Left: Calculated electron energy spectrum for $a_0 = 0.35$ at $t = 600\ \omega_p^{-1}$. Right: fundamental and Raman-shifted spectra measured at output of $Ba(NO_3)_2$ crystal. Stokes component is filtered and compressed to form seed pulse.

Figure 5 shows the experimental method that we are using to generate the required seed pulse. The main (pump) pulse at *800 nm* is produced by a conventional *4 TW* Ti:sapphire chirped pulse amplification system. The seed pulse is formed from *~10%* of the amplified, chirped *800 nm* pulse that reflects specularly from (*i.e.* into the zero-order of) the first compressor grating. This normally wasted light, still chirped, passes through a barium nitrate crystal that shifts *~10%* of its energy to a Stokes band at centered at *873 nm* by stimulated Raman scattering (SRS) (Fig. 5, right). SRS must be done with the chirped pulse to avoid continuum generation, self-focusing and other competing third-order nonlinear optical processes [20]. The shifted light is then filtered and compressed to form a seed pulse that is perfectly synchronized with the main pulse.

We now simulate situations in which the main pulse is focused to intensity $0.25 < a_0 < 0.5$, *i.e.* spot radius $15 < w_0 < 20\ \mu m$ for the pulses described above. For near-resonant ($\omega_p \approx \omega - \omega_{seed}$) plasma density, $k_p w_0 \approx 20$, so the nominal criterion $k_p w_0 >> 1$ for 1D simulation is satisfied at $t = 0$. At $t > 0$, 1D effects will continue to dominate at early times; 2D effects become important later. To estimate when the 1D $\rightarrow$ 2D transition occurs, consider the 1D effects of longitudinal bunching and photo acceleration, and the 2D effect of transverse focusing. The variations of the pulse envelope at a fixed value of the coordinate $\zeta = x - v_g t$ for the two cases are respectively given by [21]:

$$\frac{1}{<a^2>}\frac{\partial \Delta <a^2>}{\partial \tau} = \frac{i\omega_p}{\gamma_p^2}\frac{\delta n}{n} \quad \text{and} \quad \frac{1}{<a^2>}\frac{\partial^2 \Delta <a^2>}{\partial \tau^2} = -\frac{1}{\gamma_p^2}\left(\frac{c}{r}\right)^2\frac{\delta n}{n}\,. \tag{1}$$

At fixed ζ, if $\delta n/n$ is approximately constant for $0 < t < \tau$, then $\Delta<a^2>_{1D}$ grows as τ, while $\Delta<a^2>_{2D}$ grows as τ^2. The transition from 1D to 2D occurs at:

$$\tau_{transition} = \frac{4L_R}{c\gamma_p} \tag{2}$$

For example, with Rayleigh length $L_R \approx 1\ mm$ and $\gamma_p = 5.8$, $\tau_{transition} = 760\ \omega_p^{-1}$. Here we present 1D PIC simulations of wakefield acceleration up to $\tau_{transition}$.

The main and seed pulses propagate in the x-direction, and are linearly polarized in the y-direction. Their electric fields are respectively

$$E_y = E_0 f(x\text{-}x_c,\ \sigma_x,\ k),\ \text{where}\ f(\Delta x,\sigma,k) = \exp\left[-\frac{\Delta x^2}{2\sigma^2}\right]\sin kx\ ,\ \text{and}$$

$$E_y' = E_0' f(x\text{-}x_c',\ \sigma_x',\ k'),\ \text{with}\ \omega' = \omega - \omega_p\ \text{and}\ k' \approx k - k_p. \qquad (3)$$

For the simulation results below, the main pulse has $\lambda = 1\ \mu m$, pulse length $2\sigma_x = 100\ fs$, the seed pulse $\sigma_x' = \sigma_x$ and $x_c' = x_c + 0.5\sigma_x$. The cold ($T \approx 0$) plasma has density $n_e = 3.3 \times 10^{19}\ cm^{-3}$, which gives $\lambda_p = 5.8\mu$, and $\gamma_p = \lambda_p/\lambda = \omega/\omega_p = 5.8$.

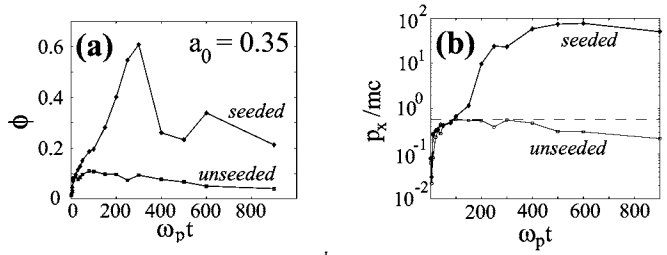

FIGURE 6. a) Wakefield potential vs t (units of ω_p^{-1}): seeded (top), unseeded (bottom); b) maximum electron momentum vs. t (units of ω_p^{-1}): seeded (top), unseeded (bottom).

Fig. 6 shows the time evolution of (a) the normalized wakefield potential $\phi = eE_x/(m\omega_p c)$ and (b) the maximum electron momentum $p_x^{\max}$ for $a_0 = 0.35$ and seed amplitude $a_0' = 0$ or $a_0' = 0.1\ a_0$. For the unseeded case, ϕ never exceeds 0.1, whereas for the seeded case ϕ reaches a maximum of 0.6 at $t = 300\ \omega_p^{-1} < \tau_{transition}$, sufficient to trap electrons [22]. $p_x^{\max}$, shown in Fig. 6b, is reached when a trapped electron accelerates from the top of the potential barrier through a half plasma wavelength, where it dephases from the wake potential. In the lab frame, in the ideal case where ϕ is constant over the course of acceleration, the maximum dephasing time is $t_{deph} = 2\pi\gamma_p^2/\omega_p$ and maximum kinetic energy $KE_{max} = 4\gamma_p^2\phi_0 mc^2$ [23].

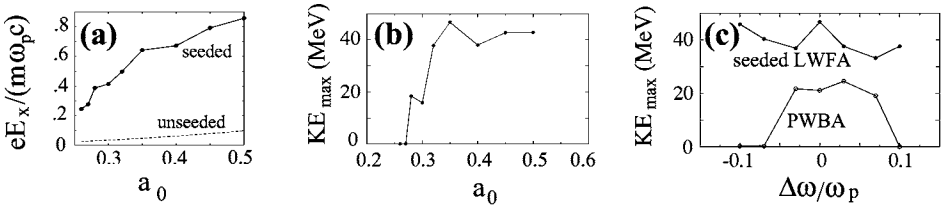

FIGURE 7. (a) Maximum wakefield amplitude vs a_0: seeded (top), unseeded (bottom). (b) KE_{max} vs. a_0 for seeded LWFA. (c) KE_{max} vs. frequency detuning: seeded LWFA (top) vs. beat wave (bottom).

Figure 7 shows how (a) ϕ_{max} and (b) KE_{max} scale with a_0 for seeded SM-LWFA, while maintaining seed amplitude $a_0' = 0.1\ a_0$. The threshold for electron trapping and acceleration to MeV energies is near $a_0 \sim 0.28$. KE_{max} rises steadily up to $a_0 \approx 0.35$, then saturates, despite continuing increase of ϕ, indicating deviation from the ideal case described above. Those electrons that reach $KE_{max} \sim 42\ MeV$ are accelerated before $t_{deph} \sim 211 < \tau_{transition}$, so the 1D approximation remains valid. The yield of MeV electrons can be derived for experimental parameters of interest. For example, if $a_0 = 0.35$ is realized experimentally with a main pulse of energy $170\ mJ$, duration $100\ fs$, focused to $w_o = 18\mu m$, our simulations predict that $1.3\ nC$ per

pulse of electrons with $KE > 1\ MeV$ are produced. The corresponding electron spectrum at $t = 600$ ($x \sim 554\ \mu m$), is shown at the left side of Figure 5.

The Raman-seeded SM-LWFA superficially resembles the plasma beat-wave accelerator (PBWA) [23]. However, the two approaches differ markedly in the ratio $b = I_{seed}/I_{main}$, which is 0.01 for the simulations above, and ~ 1 for the PBWA. This, in turn, leads to two important distinctions between the two methods. First, the smaller ratio $b \sim 0.01$ is much easier to realize experimentally, since only a small fraction of the main pulse need be converted to the Stokes wavelength. Secondly, the growth of the Raman-seeded wakefield is much less sensitive than PBWA to detuning $\Delta\omega = \omega_{seed} - (\omega - \omega_p)$ of the seed pulse frequency from its optimum value $\omega_{seed} = \omega - \omega_p$, as illustrated in Fig. 7c. This plot compares KE_{max} vs $\Delta\omega/\omega_p$ for the Raman-seeded LWFA and PBWA. For this comparison, we assumed a common primary pulse with intensity I_0 was split into a main pulse with $I_{main} = (1-\alpha)I_0$ and a seed pulse with $I_{seed} = \alpha\eta I_0$, where η is the conversion efficiency into the Stokes frequency. Thus $b = \eta\alpha/(1-\alpha) = 0.01$ and $a_0 = 0.356$ for the Raman-seeded LWFA example (using $\alpha = 0.032$, $\eta = 0.3$), which yields the electron spectrum shown in Fig. 5 (left) and $1.3\ nC/pulse$ as discussed above, while $b = 1$ and $a_{0,main} = a_{0,seed} = 0.171$ for the PBWA example (using $\alpha = 0.769$, $\eta = 0.3$). KE_{max} is consistently higher for the seeded case than for the PBWA. More importantly, the seeded LWFA is more stable against deviation of the seed pulse frequency from $\omega - \omega_p$. Evidently, the detuned seed pulse self-corrects more quickly as self-modulation evolves when b is small. Thus the Raman-seeded LWFA is much more compatible than PBWA with plasmas of nonuniform density, such as those present in a gas jet. As b decreases from unity, the maximum KE plot evolves continuously from the narrow plot shown for the PBWA to the broader seeded LWFA curve. Of course, b cannot decrease indefinitely below 0.01, because the production rate of energetic electrons then falls eventually to the level of the unseeded SM-LWFA.

ACKNOWLEDGMENTS

We are grateful to Toshi Tajima for inspiration, encouragement and many discussions in connection with all of the work presented here. This research is supported by U. S. Department of Energy grant DEFG03-96ER40954.

REFERENCES

1. Andreev, N. E., Gorbunov, L. M., Kirsanov, V. I., Nakajima, K., and Ogata, A., *Phys. Plasmas* **4**, 1145 (1997).
2. Dorchies, F., Marquès, J. R., Cros, B. et al., *Phys. Rev. Lett.* **82**, 4655-4658 (1999).
3. Ehrlich Y., Cohen C., Zigler A., Krall, J., Sprangle, P., and Esarey, E., *Phys. Rev. Lett.* **77**, 4186-4189 (1996); Hosokai T., Kando, M., Dewa H., Kotaki, H., Kondo, S., Hasegawa, N., Nakajima, K., Horioka, K., *Opt. Lett.* **25**, 10-12 (2000); Spence D. J. and Hooker, S. M., *Phys. Rev. E* **63**, 015401 (2001).
4. Durfee, C. G. Lynch, J. and Milchberg, H. M. *Phys. Rev. E* **51**, 2368-2388 (1995); Clark, T. R. and Milchberg, H. M., *Phys. Rev. Lett.* **78**, 2373-2376 (1997).
5. Gaul, E. W., LeBlanc S. P., Rundquist, A. R., Zgadzaj, R., Langhoff, H. and Downer, M. C., *Appl. Phys. Lett.* **77**, 4112-4114 (2000).
6. Siders, C.W., Le Blanc, S. P., Fisher, D., Tajima, T., Downer, M. C., Babine, A., Stepanov, A., Sergeev, A., *Phys. Rev. Lett.* **76**, 3570-3573 (1996); Marquès, J. R., Dorchies, R., Amiranoff, F., Audebert, P., Gauthier, J. C., Geindre, J. P. , Antonetti, A., Antonsen, T. M., Chessa, P., Mora P., *Phys. Plasmas* **5**, 1162-1170 (1998); Le Blanc, S. P., Gaul, E. W., Matlis, N. M., Rundquist, A. R., Downer, M. C., *Opt. Lett.* **25**, 764-766 (2000).
7. Wilks S. C., Dawson J. M., Mori W. B., Katsouleas T., Jones M. E,. *Phys. Rev. Lett.* **62**, 2600-2603 (1989).
8. Dias J. M., Oliveira e Silva, L., and Mendonca, J. T., in *Proceedings of the 1st JAERI-Kansai International Workshop on Ultrashort-Pulse Ultrahigh-Power Lasers and Simulation for Laser-Plasma interactions* (JAERI-Conf. 98-004, 1997), pp. 1-24; Dias J. M., Stenz C. Lopes N., Badiche X., Blasco F., Dos Santos A., Oliveira e Silva L., Mysyrowicz A., Antonetti A., and Mendonca J. T. *Phys. Rev. Lett.* **78**, 4773-4776 (1997).
9. Davies, J. R. and Mendonca, J. T., *Phys. Rev. E* **62**, 7168-7180 (2000); Marcatili, E. A. J. and Schmeltzer, R. A., *Bell Syst. Tech. J.* **43**, 1783-1809 (1964).

10. Nikitin, S. P., Alexeev, I., Fan, J., and Milchberg, H. M., *Phys. Rev. E* **59**, R3839-3842 (1999); Volfbeyn, P., Esarey, E. and Leemans, W. P., *Phys. Plasmas* **6**, 2269-2276 (1999).
11. Andreev, N., Chegotov, M. V., Downer, M. C., Gaul, E. W., Matlis, N. M., Pogosova, A. A., and Rundquist, A. R., *IEEE Trans. Plasma Sci.* **28**, 1090-1097 (2000).
12. Miller, D. R., "Free Jet Sources," in *Atomic and Molecular Beam Methods*, Vol. 1, edited by G. Scoles, Oxford University Press, New York, 1988, pp. 14-53.
13. Bird, G. A., *Molecular Gas Dynamics and the Direct Simulation of Gas Flows*, Oxford University Press, New York, 1994.
14. Ammosov, M.V., Delone, N. B., Krainov, V. P., *Sov. Phys. JETP* **64**, 1191-1194 (1986).
15. Bagnoud, V. and Salin, F., *Applied Physics B* **70**, S165-S170 (2000).
16. Tajima, T., *J. Jpn. Soc. Therap. Rad. Oncol.* **9**, 2-5 (1997); Hogstrom, K., private communication, 2002.
17. Leemans, W. P. , Rodgers, D., Catravas, P. E., Geddes, C. G. R., Fubiani, G., Esarey, E., Shadwick, B. A., Conahue, R., and Smith, A., *Phys. of Plasmas* **8**, 2510-2277 (2001).
18. Pitthan, R., private communication, 2002.
19. Fisher, D. L. and Tajima, T., *Phys. Rev. E* **53**, 1844-1851 (1996).
20. Zhavoronkov, N., Noack, F., Petrov, V., Kalosha, V. P. and Herrmann, J., *Opt. Lett.* **26**, 47-49(2001).
21. Mori, W. B., *IEEE J. Quant. Elec.* **33**, 1942-953 (1997).
22. Esarey, E. and Pilloff, M., *Phys. Plasmas* 2, 1432-1440 (1995).
23. Esarey, E., Sprangle, P., Krall, J. and Ting, A., *IEEE Trans. Plasma Sci.* **24**, 252-286 (1996).